

Theoretical prediction of pre-supernova neutrinos and their detection

C. Kato^{1,3}, K. Ishidoshiro² and T. Yoshida³

¹Department of Aerospace Engineering, Tohoku University, Sendai 980-8579, Japan; e-mail: chinami.kato.e8@tohoku.ac.jp

²Research Center for Neutrino Science, Tohoku University, Sendai 980-8578, Japan; e-mail: koji@awa.tohoku.ac.jp

³Department of Astronomy, Graduate School of Science, The University of Tokyo, Tokyo 113-0033, Japan; e-mail: tyoshida@astron.s.u-tokyo.ac.jp

Xxxx. Xxx. Xxx. Yyyy. AA:1–27

This article's doi:
10.1146/(please add article doi)

Copyright © YYYY by Annual Reviews.
All rights reserved

Keywords

Neutrino, Massive star, Stellar evolution, Supernova

Abstract

Almost 30 years have passed since the successful detection of supernova neutrinos from SN 1987A. In the last decades, remarkable progress has been made in neutrino detection technique, through which it may be possible to detect neutrinos from a new source, pre-supernova (pre-SN) neutrinos. They are emitted from a massive star prior to core bounce. Because neutrinos escape from the core freely, they carry information about the stellar physics directly. Pre-SN neutrinos may play an important role in verifying our understanding of stellar evolution for massive stars. Observations of pre-SN neutrinos, moreover, may serve as an alarm regarding a supernova explosion a few days in advance if the progenitor is located in our vicinity, enabling us to observe the next galactic supernova. In this review, we summarize the current status of pre-SN neutrino studies from both of the theoretical and observational points of view.

Contents

1. INTRODUCTION	2
2. THEORY OF PRE-SUPERNOVA NEUTRINOS	4
2.1. Massive Star Evolution	4
2.2. Neutrino emission	6
2.3. Luminosities and spectra of pre-SN neutrinos	8
2.4. Neutrino oscillation	11
3. PRE-SUPERNOVA NEUTRINO DETECTION AND SN ALARM	12
3.1. Detectors and pre-SN neutrino observations	12
3.2. Detector sensitivity	14
3.3. Early alarm with pre-supernova neutrino	18
4. FINDINGS FROM FUTURE OBSERVATIONS	19
4.1. Distinction of progenitor models for core-collapse supernovae	19
4.2. Restriction on convective properties	21
4.3. Determination of neutrino mass ordering	21
5. SUMMARY AND FUTURE PROSPECTS	22
5.1. Summary	22
5.2. Future prospects	24

1. INTRODUCTION

A big breakthrough came in neutrino observations in 1987. A massive star exploded in the Large Magellanic Cloud, which is located at ~ 50 kpc from the Earth. Such a big explosion at the end of the life of a massive star is called a "supernova". KAMIOKANDE-II, Irvine-Michigan-Brookhaven, and Baksan, which were neutrino detectors running at that time, detected ~ 11 , 8 and 5 neutrinos, respectively, accompanying "SN 1987A" (1, 2, 3). From their data, the average energy of electron anti-neutrinos ($\bar{\nu}_e$'s) was found to be ~ 15 MeV, and the energy released was $\sim 8 \times 10^{52}$ ergs (1). These outcomes were consistent with the neutrino heating mechanism, which is one of the most favored explosion mechanisms (4). This discovery advanced our understanding of supernova explosions.

In the last few decades, remarkable progress has been made in neutrino detection techniques. Neutrino detectors with large volumes and low-energy thresholds for neutrinos have been running such as Super-Kamiokande (SK) and Kamioka Liquid-scintillator Antineutrino Detector (KamLAND). A further scale-up will be realized in future detectors such as Hyper-Kamiokande (HK) and Jiangmen Underground Neutrino Observatory (JUNO). It is worth mentioning the low background techniques that use a delayed coincidence (DC) for inverse- β decay (IBD) to confirm the events via prompt and delayed signals with the temporal and spatial correlations. The SK-Gd project (Super-Kamiokande with gadolinium) uses such techniques (5). Past and current neutrino detectors are mainly sensitive to $\bar{\nu}_e$'s, whereas newer detectors with the ability to detect other flavors may become available in the near future. For the detection of electron neutrinos (ν_e 's), the Helium and Lead Observatory (HALO) is running at SNOLAB based on neutrino reactions on lead (6), and Deep Underground Neutrino Observatory (DUNE) is currently under

construction at Sanford Underground Research Facility (SURF) (7). The detection of heavy-lepton neutrinos (ν_x 's) can be realized by the observation of coherent elastic neutrino-nucleus scattering (CE ν NS), as in the COHERENT experiment at the Spallation Neutron Source (8). Sensitivity of dark matter detectors to ν_x 's via CE ν NS is discussed in References (9, 10, 11). Multi-flavor studies for astrophysical neutrino sources will be available soon.

Such developments may enable the detection of neutrinos from new sources. "Pre-supernova (pre-SN) neutrinos", which are mainly emitted from a core of a massive star but prior to core bounce, are one candidate. Massive stars are thought to be the progenitors of core-collapse supernovae (CCSNe) (e.g., 12). They evolve with synthesizing heavier elements like He, C, Ne, O, Si and Fe via nuclear burnings. Efficient neutrino emission occurs by thermal emission processes in a stellar core with high temperature and density after a carbon core is formed. The nuclear weak processes [i.e., electron capture (EC), in which an electron is captured by a nucleus and a nuclear proton is changed to a neutron and β processes] enhance neutrino emission after iron-group elements are synthesized. Neutrinos cool down the core and have important roles in its thermal evolution.

The possibility of pre-SN neutrino detection was first proposed by Odrzywolek *et al.* (13). They calculated the luminosities and spectra of the neutrinos emitted via electron-positron pair annihilation for a $20 M_{\odot}$ progenitor model and estimated the detection events for six neutrino detectors. Assuming that the distance to a supernova is 1 kpc, the event numbers would be 41 for SK and, 4 for KamLAND. This work, a pioneer of qualitative calculations for pre-SN $\bar{\nu}_e$'s, enables our discussions of "pre-SN neutrino astronomy".

Recent studies have employed state-of-the-art stellar evolution models to calculate the time evolution of the number luminosities and spectra for pre-SN neutrinos (14, 15, 16, 17). In addition, a variety of neutrino reactions are included in their calculations. Another thermal process—namely a plasmon decay—becomes dominant in the late phases of some progenitors (14). It also has been pointed out that neutrino emissions via nuclear weak interactions may dominate over the thermal processes just prior to collapse (16, 17, 18).

Pre-SN neutrino astronomy may clarify current uncertainties in massive stars and supernovae. First, the detection of pre-SN neutrinos can be a direct observation of stellar interiors. The investigation of stellar evolutions has a long history, and a standard model has almost been established. Stellar physics, however, still has many uncertainties. Pre-SN neutrinos may be one of the most promising tools to look in stellar physics because they can propagate through stars freely and can be detected without losing the thermal information of the core. It has been reported that pre-SN neutrino observations will make it possible to distinguish between the two types of CCSN-progenitors—iron core collapse supernovae (FeCCSNe) and electron capture supernovae (ECSNe)—(14) and to impose restrictions on convective properties associated with oxygen-shell (O-shell) and silicon-shell (Si-shell) burnings (15). Second, the observation of pre-SN neutrinos serves as an alarm (SN alarm) regarding the subsequent explosion, and makes it possible to observe the next galactic supernova. The neutrinos may be detected a few days before the explosion, if the progenitor is located in our vicinity (< 1 kpc) (16, 19). It is supposed that galactic supernovae occur once every few hundreds years. Thus, the SN alarm has an important role in helping us understand the mechanism of supernova explosions. We believe that the detection of pre-SN neutrinos in the future will have an impact as big as that of the historical neutrino events at SN 1987A.

In this review, we introduce pre-SN neutrinos from both the theoretical and observational points of view. We first summarize the evolutions of massive stars and neutrino emission in Section 2. We then show the current status of neutrino detectors and discuss a pre-SN neutrino alarm in Section 3. Section 3 also provide the expected numbers of pre-SN neutrino events in current and future detectors. In Section 4, we discuss what can be learnt from future observations of pre-SN neutrinos; we focus on the distinction of supernova progenitors, the restrictions on shell burnings, and the determination of the neutrino mass ordering. Finally, we summarize the review and mention the future prospects of pre-SN neutrino studies in Section 5.

2. THEORY OF PRE-SUPERNOVA NEUTRINOS

2.1. Massive Star Evolution

Massive stars—that is, stars with masses heavier than $\sim 8 M_{\odot}$ at the zero-age main sequence (ZAMS)—start their lives with hydrogen burning and end by a dynamical collapse of the central cores (e.g., 20, 21). There are two types of progenitors that produce CCSNe. In most cases, the stellar core is mainly composed of iron (Fe core), and its collapse leads to an FeCCSN. In other cases, which account for $\sim 5\%$ of all CCSNe according to a recent study (22), the core is composed of oxygen and neon (ONe core), and an ECSN occurs at the end. The initial mass of main sequence stars is the primary factor determining which state is obtained in the end: Less massive stars (mass less than $\sim 9.5 M_{\odot}$) will lead to ECSNe, and more massive stars will produce FeCCSNe (23, 24, 25, 26). We explain the evolution sequence of a $15 M_{\odot}$ model (15, 16) as an example of an FeCCSNe-progenitor. We then focus on the differences in evolution between the two types of progenitors, since they pass through quite different paths, as shown in Figure 1.

In the main sequence of massive stars, hydrogen is burned into helium via CNO cycles. The ignition temperature for hydrogen burning is $\sim 4 \times 10^7$ K, and it lasts for $\sim 10^7$ yr for the $15 M_{\odot}$ model. Stars in this phase are observed as blue supergiants. After the central hydrogen is exhausted, the core contracts and has an isothermal structure. Its surrounding hydrogen-shell burning makes the pressure gradient larger at the bottom of the hydrogen shell and extends the hydrogen envelope. Such a star is called a red supergiant (RSG).

Helium ignites at a core temperature of $\sim 1.5 \times 10^8$ K. This process proceeds by a triple-alpha reaction ${}^4\text{He}(\alpha\alpha, \gamma){}^{12}\text{C}$ and some of this ${}^{12}\text{C}$ converts into ${}^{16}\text{O}$ by ${}^{12}\text{C}(\alpha, \gamma){}^{16}\text{O}$ reaction. The helium core burning lasts for $\sim 1.3 \times 10^6$ yr in the $15 M_{\odot}$ model, and a carbon-oxygen core (CO core) is formed. After the depletion of helium at the core, the star moves on to a helium-shell burning stage. In this convective helium layer, 1-10% of the helium is burned into carbon.

Stars of high mass and metallicity experience a strong wind mass-loss in the RSG phase, which strips their hydrogen envelope and helium layer (27). These stars form Wolf-Rayet (WR) stars, which have smaller radii and higher surface temperatures than do RSGs. WR stars are also produced through the violent interaction with companions in binary systems.

In a massive star, the temperature reaches the threshold for carbon burning during the contraction of the CO-core. The central temperature becomes $\sim 7 \times 10^8$ K at the onset of carbon burning, and the carbon burning lasts for ~ 1800 yr in the $15 M_{\odot}$ model. An ONe core is formed by the production of ${}^{20}\text{Ne}$ and ${}^{24}\text{Mg}$ via ${}^{12}\text{C}+{}^{12}\text{C}$ fusion reactions. This is followed by several phases of carbon-shell burning for 500 yr, and this carbon-shell burning extends the

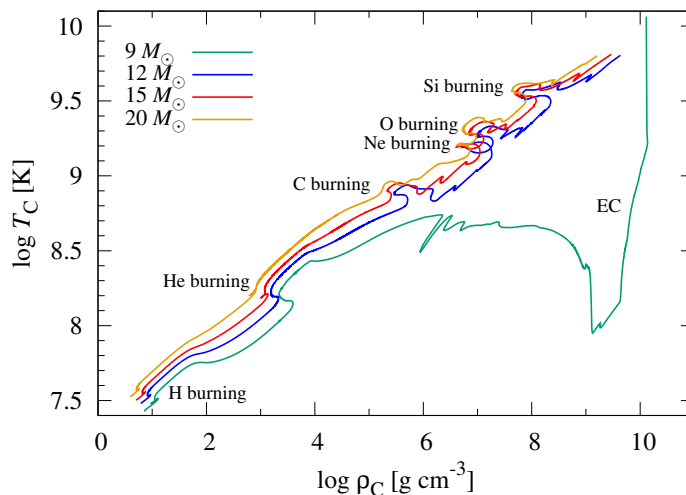


Figure 1

Evolutionary paths in the central density (ρ_C) and temperature (T_C) plane. The figure shows 12 (M_\odot , blue), 15 (M_\odot , red) and 20 (M_\odot , orange) progenitors of FeCCSNe and a 9 (M_\odot , green) progenitor of ECSNe.

ONe core. The energy released by neutrinos becomes important at this stage. The dominant emission process in massive CO cores is pair annihilation. In some lighter stars with higher electron degeneracy, the contribution of plasmon decay becomes larger for neutrino cooling in the central region. These neutrinos efficiently cool down the core and suppress further increase of the central temperature. Carbon burning then begins at an off-center part of the core, and its burning front gradually moves to the center. The 9 M_\odot progenitor in Figure 1 depicts a lower central temperature at the carbon burning phase compared with the other progenitors.

Neon ignites when the central temperature reaches $\sim 1.4 \times 10^9$ K. Neon 20 is decomposed into ^{16}O and ^4He via photo-disintegration and is also converted to ^{24}Mg and ^{28}Si through α -capture reactions. The neon core burning continues for ~ 1 yr in the 15 M_\odot model, and the core is mainly composed of oxygen and silicon (OSi core).

When the central temperature reaches 1.6×10^9 K, oxygen core burning starts. In the 15 M_\odot star model, it takes 9 and 14 months for the contractions of the OSi core and the oxygen core burning, respectively. Oxygen fusion reactions and subsequent reactions produce Si, S, and other intermediate elements. A silicon core (Si core) is then formed and grows through further O-shell burnings.

After the Si core gradually contracts for 2 months, Si-core burning, and an Fe core is formed that consists of iron-group elements. The central temperature reaches $\sim 3 \times 10^9$ K at this time. Silicon is almost depleted in 4.5 days in the 15 M_\odot model, and the Fe core and surrounding Si-rich layers grow up through Si-shell and O-shell burnings, respectively. During contraction of the Fe core, the iron-group elements start to be photo-disintegration, which is an endothermic reaction. In addition, neutrinos are emitted by EC reactions in the Fe core, where nuclear statistical equilibrium (NSE) is achieved. In the NSE region, the system reaches the minimum of its free-

energy and the nuclear composition is unchanged on the same matter condition. These reactions reduce the electron fraction and in turn the electron degenerate pressure decreases. These two phenomena enhance core contraction, and the central core begins to collapse 21 hours after silicon core burning. At a certain point in the Si-shell burning, EC dominates pair annihilation, which is the main emission process until this time (16).

If the mass of the ONe core is smaller, the evolution at neon burning is different from that of normal massive stars (28, 29, 30). The increase in the central temperature is suppressed even during core contraction because of the strong cooling by neutrino emission via plasmon decay. The neon ignition hence occurs at an off-center region and causes strong neon-shell burning. A convective OSi layer is formed around the ONe core. The burning front gradually moves inward, and the neon burning moves to the off-center oxygen burning. If the burning front reaches the center before silicon burning starts, an OSi core is formed. Silicon burning also occurs at an off-center region, and an Fe-layer is formed on the ONe or Si core. The Fe layer forms the Fe core when the burning front reaches the center. The central core begins to collapse in the same manner as that of more massive ONe cores.

When the mass of the ONe core is smaller than the critical mass for neon ignition, $1.35 - 1.37 M_{\odot}$ (31, 32, 33), the maximum temperature of the star does not reach the threshold for neon ignition, and the ONe core continues to contract. In this case, the star evolves to a super asymptotic giant branch star. During this phase, the ONe core grows through helium-shell and carbon-shell burnings, while the hydrogen envelope is stripped away by a strong mass loss (34). When the total mass of the star becomes smaller than the critical mass, the star gradually cools down to an ONe white dwarf (WD). In contrast, when the ONe core mass of such a star exceeds the critical mass, the star becomes an ECSN. The lowest initial mass for ECSN-progenitors is suggested to be $\sim 8 - 9.5 M_{\odot}$, and it depends on the treatment of a convective boundary (26). The $9 M_{\odot}$ progenitor in Figure 1 is an example of this evolutionary path. The central temperature decreases by neutrino emission via plasmon decays and increases again up to $\sim 2 \times 10^9$ K, which is the threshold for neon ignition, through ECs of ^{23}Na , ^{24}Mg , ^{24}Na , ^{20}Ne , and ^{20}F during core contraction (e.g., 35, 25, 24). This is accelerated by the successive oxygen and silicon burning, and the temperature exceeds 10^{10} K. Deflagration starts to propagate outward to convert the ONe core to an Fe core (31, 25, 36). The Fe core then collapses to an ECSN. The explosion of ECSNe is expected to be weaker than that of FeCCSNe. However, it is difficult to distinguish it from that of low-mass FeCCSNe. A thermal explosion by the propagation of deflagration waves is another possibility for ECSNe (37). In this case, a part of the outer layer could be blown off, with an ONe(Fe) WD left as a remnant. This scenario seems to be favorable for stars with low central densities at neon ignition (38).

2.2. Neutrino emission

Pre-SN neutrinos have a key role in the evolutions of massive stars because they are efficiently emitted from the stellar core, taking energy away. Neutrino reactions are mainly classified into thermal pair emission and nuclear weak interactions. Neutrino luminosities from thermal emission dominate the photon luminosity after carbon burning begins; nuclear weak interactions enhance neutrino emission after heavy element synthesis has commenced.

2.2.1. Thermal pair emission. There are four processes responsible for neutrino emission:

- electron-positron pair annihilation (pair)



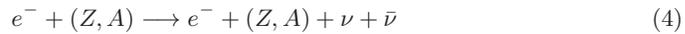
- plasmon decay (plasmon)



- photo neutrino (photo)



- bremsstrahlung (brems)



In the above expressions, Z and A are the atomic number and the mass number of nuclei, respectively. These processes produce all flavors of neutrinos. The reaction rates depend mainly on three hydrodynamical variables: density ρ , temperature T and electron fraction Y_e (or chemical potential of electrons). Having in mind applications to stellar evolution calculations, Itoh *et al.* (39) obtained useful fitting formulas for the energy loss rates in these processes. They also investigated which reaction is dominant for a given combination of density and temperature. According to their results, pair annihilation and plasmon decay are the most important neutrino emission processes in the evolutions of massive stars. This finding has been confirmed by other works (18, 14, 17, 40).

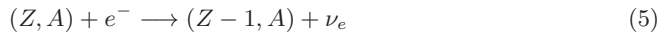
The emissivity of pair annihilation is highly sensitive to temperature with the increase in the number of electron-positron pairs. The dependence on ρY_e is much less drastic: The emissivity decreases with its value because the number of electron-positron pairs is reduced due to the Fermi-degeneracy of electrons. The number spectrum of plasmon decay neutrino emission is much less sensitive to temperature than for pair annihilation, but it depends more on ρY_e . The peak energy is considerably smaller in plasmon decay. This fact has an important implication for regarding observability of the neutrinos emitted by this process in neutrino detectors.

It should be noted that we do not get neutrino spectra directly from calculations of stellar evolutions. Hence, we evaluate the luminosities and spectra of neutrinos in post processing; that is, we extract the profiles of hydrodynamical variables from stellar evolution calculations. Because stars are not homogeneous, we first derive the reaction rates $R(E_\nu, E_{\bar{\nu}}, \cos \theta)$, employing local hydrodynamical variables with the energies of neutrino and anti-neutrino $E_\nu, E_{\bar{\nu}}$ and the angle between the directions of the neutrino pair θ . The numerical formulas for pair annihilation (41, 42) and plasmon decay (43) have been established previously. The local spectra for neutrinos and anti-neutrinos are simply given as integrals of the reaction rates R over the angle and the energy of the partner. Finally, the number spectrum dL_N^ν/dE_ν is obtained by integration of the local spectra over the star. The number luminosity L_N^ν is a product of the integration of the number spectrum over neutrino energy.

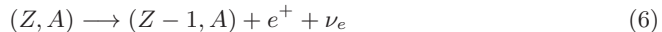
2.2.2. Nuclear weak interaction. After the silicon burning, nuclear weak interactions can no longer be neglected. In particular, once initiated, EC on heavy nuclei is the dominant reaction.

It plays an important role in the hydrodynamics of core collapse. Although β^+ decays of heavy nuclei also emit ν_e 's, they are certainly sub-dominant. $\bar{\nu}_e$'s are emitted either by positron capture (PC) or β^- decay.

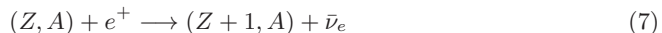
- electron capture (EC)



- β^+ decay



- positron capture (PC)



- β^- decay



The reaction rates for these reactions have been calculated in several works [e.g. FFN (44), ODA (45), LMP (46), LMSH (47)]. The energy spectrum for a respective reaction is reconstructed by the effective Q -value method, using the reaction rates and the average energy of neutrinos (See details in References (48, 49, 17)).

2.2.3. Electron capture on free protons. Although not abundant, EC on free protons:



can not be ignored, since the cross section is larger than that of ECs on heavy nuclei (46). We normally employ the reaction rate calculated by Bruenn *et al.* (50) in this process.

2.3. Luminosities and spectra of pre-SN neutrinos

In this section, on the basis of a model from Kato *et al.* (16) we introduce typical properties of pre-SN neutrinos. This model considers neutrino emission during both the quasi-static evolutions of progenitors and the hydrodynamical core collapse until $\rho_c = 10^{13} \text{ g cm}^{-3}$. For the former, they use the stellar evolution model with $15 M_\odot$, whereas for the latter they conduct a one-dimensional simulation under spherical symmetry to solve radiation-hydrodynamic equations (51). It is important to take into account neutrino transport in the core properly, once the density becomes high enough to trap neutrinos. The two evolutionary phases are mutually connected when the central density becomes $\rho_c = 10^{10.3} \text{ g cm}^{-3}$, which corresponds to $t \approx 0.1 \text{ s}$ before core bounce. The top-left panel of Figure 2 shows the time evolution of number luminosities. The number luminosity of ν_e 's (black, dotted) gradually increases up to $\sim 10^{55}$ and 10^{57} s^{-1} just before core collapse and core bounce, respectively. EC on heavy nuclei (blue, dotted) and free protons (cyan, dotted) makes large contributions to the total luminosity. The ν_e emission occurs predominantly in the collapse phase ($t < 0.1 \text{ s}$), although this phase is much shorter than the progenitor phase that precedes it. For $\bar{\nu}_e$'s, the number luminosity (red, solid) reaches a maximum $L_N^\nu \sim 10^{53} \text{ s}^{-1}$ at the beginning of the core collapse. Neutrino emission via pair annihilation (green, solid) dominates the other reactions at $t > 400 \text{ s}$, whereas after this, β^- decay

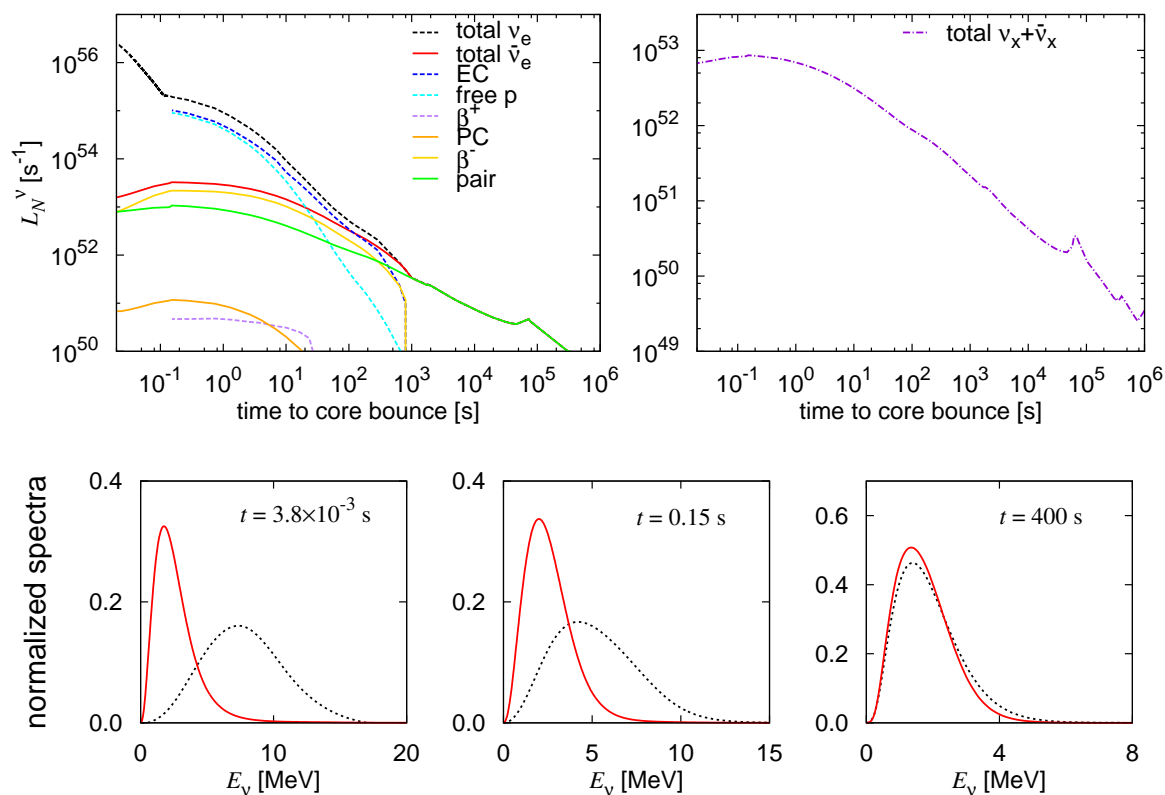


Figure 2

Top: Time evolution of number luminosities for the emission processes of $\bar{\nu}_e$'s (solid) and ν_e 's (dotted) in the left panel and for that of ν_x 's and $\bar{\nu}_x$'s in the right panel for the Kato model (16). All luminosities of heavy-lepton (anti-)neutrinos are summed up. Time is measured from core bounce and different colors denote different emission processes. We switch from the quasi-static calculation of stellar evolution to the hydrodynamical simulation for the core-collapse phase at $t \sim 10^{-1}$ s. For ν_e 's in the collapse phase, only the total luminosity is shown because it is all that the transport calculations produce. Bottom: Snapshots of the number spectra for $\bar{\nu}_e$'s (red, solid) and ν_e 's (black, dotted) at $t = 3.8 \times 10^{-3}$, 0.15 and 400 s. They are normalized by the number luminosities L_N^ν at each time point. Neutrino oscillations are not included in all panels of this figure.

(yellow, solid) overcomes it. Because of the Fermi-blocking of electrons in the final state, β^- decay is suppressed at high densities, at which electrons are strongly degenerate, and the number luminosity of $\bar{\nu}_e$'s decreases, eventually leading to core bounce. As a consequence, the progenitor phase is dominant over the collapse phase in $\bar{\nu}_e$ emission. The total number luminosity of ν_x 's is shown in the top-right panel of Figure 2. Because ν_x 's are only emitted via pair annihilation in this phase, the luminosity is much smaller than those of ν_e 's and $\bar{\nu}_e$'s. It is difficult for currently operational as well as planned detectors to detect ν_x 's. They are, however, converted to ν_e 's

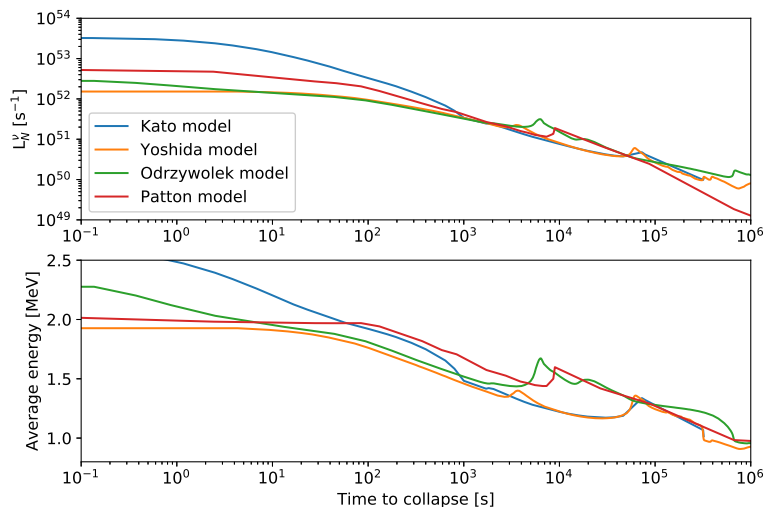


Figure 3

Time evolution of number luminosities (top) and average energies (bottom) of $\bar{\nu}_e$'s for four pre-SN neutrino models (15, 16, 53, 54). Neutrino oscillations are not included.

or $\bar{\nu}_e$'s through neutrino oscillation, and they affect the fluxes of other neutrino flavors on the Earth (see Section 3.2).

Time snapshots of the neutrino spectra at $t = 3.8 \times 10^{-3}$, 0.15 and 400 s are shown in the bottom panels of Figure 2. At $t = 400$ s, the dominant reaction for $\bar{\nu}_e$'s changes, while the other two time points correspond respectively to the times just before core collapse and core bounce. The average energy of ν_e 's reaches ~ 8 MeV before core bounce, whereas that of $\bar{\nu}_e$'s remains ~ 3 MeV. The difference in neutrino flavors is caused by the difference of the degeneracy between electrons and positrons. The results of the Kato model are available at (52), and readers may refer to these data for the time evolution of neutrino spectra.

The properties of pre-SN neutrinos depend on stellar models and neutrino processes employed in calculations. In this review, we focus on four representative models for pre-SN neutrinos, the Kato (16), Yoshida (15)¹, Odrzywolek (54)² and Patton (53) models³. The four models employ different stellar models; Takahashi models (15, 16) calculated using HOSHI code (55, 56, 36, 57) for the first two and Woosley (20) and MESA models (58) for the latter two. The Odrzywolek and Yoshida models take only pair annihilation into their calculations, whereas the Kato and Patton models also include nuclear weak interactions. Figure 3 shows the time evolutions of the number luminosities (top) and average energies of $\bar{\nu}_e$'s (bottom) for the different stellar

¹<https://doi.org/10.5281/zenodo.3778014>

²<http://th.if.uj.edu.pl/odrzywolek/psns/index.html>

³<https://doi.org/10.5281/zenodo.2598709>

models with $15 M_{\odot}$. Here, we focus on the evolution until core collapse. We find that the number luminosities of the Kato and Patton models are larger than those of the other two because of nuclear weak interactions. Even though both the Kato and Patton models take the same nuclear weak interactions into account, their luminosities and average energies have large differences at $t < 100$ s. This seems to be due to the different treatments of the mass fractions of nuclei. In the Patton model, mass fractions derived from solving nuclear networks with 204 isotopes in both NSE and non-NSE regions have been adopted, whereas the Kato model adopts NSE compositions recalculated for 3928 nuclei with Furusawa equation of state (59) in post processing. The Odrzywolek and Yoshida models, in which only pair annihilation is included, have similar number luminosities except for at $t < 5$ s. The deviations in number luminosities and average energies between the two models at $t < 5$ s seemingly come from the difference in progenitor models, but detailed investigation is necessary to make conclusive remarks. We also find two peaks in the number luminosities at $t \sim 5 \times 10^3$ and 5×10^4 s, which correspond to the Si-shell and O-shell burnings, respectively (See Section 4.2). Features such as amplitudes and widths of peaks depend on the pre-SN neutrino models. Because these peaks will be confirmed by pre-SN neutrino observations (15), a detailed comparison of shell burnings among these models is required. It should be noted that the origin of the time may be changed due to the theoretical uncertainties in the definition of core collapse.

In any case, pre-SN neutrinos are smaller in number and have lower energies compared with supernova neutrinos, for which $L_N^{\nu} \sim 10^{58} \text{ s}^{-1}$ and $\langle E_{\nu} \rangle$ is in the order of tens MeV (60). Therefore, we need detectors with high sensitivity to low-energy neutrinos and with a low background for the detection of pre-SN neutrinos.

2.4. Neutrino oscillation

Neutrinos have small but finite masses (e.g., 61, 62, 63) and can convert their flavors during propagation when mass eigenstates and flavor eigenstates do not match. This phenomenon is called a neutrino oscillation and affects neutrino fluxes. Its behavior depends on the surrounding condition. Two types of oscillation—vacuum oscillation and Mikheyev-Sumirnov-Wolfenstein (MSW) effect via electron forward-scattering (64)—should be taken into account in the pre-bounce phase. In the MSW effects, the effective mixing angles depend on the electron number density and reach their maximum at resonance points. They are located near the boundaries C-He and He-H layers. Neutrinos are mainly produced inside the resonance points and certainly pass through them. The mass eigenstate of $\bar{\nu}_e$'s is $\bar{\nu}_{m1}$ and $\bar{\nu}_{m3}$ at birth in the normal and inverted mass orderings, respectively, where $\bar{\nu}_{mi}$ is the i -th mass eigenstate of anti-neutrinos. In the pre-bounce phase, the density scale height at the resonance points is longer than the oscillation length. The adiabatic approximation is therefore available, and the transition of mass eigenstates never occurs, irrespective of the progenitor types (14). Note that collective oscillation (e.g., 65) induced by neutrino self-interaction is negligible here because neutrinos can freely escape from a star, and the self-interaction hardly occurs.

If we take two oscillations into account, the flux of pre-SN $\bar{\nu}_e$'s on the Earth is shown as (66),

$$F_{\bar{\nu}_e}(E_{\nu}, t, d) = pF_{\bar{\nu}_e}^0(E_{\nu}, t, d) + (1 - p)F_{\bar{\nu}_x}^0(E_{\nu}, t, d), \quad (10)$$

where $F_{\bar{\nu}_\alpha}^0(E_{\nu}, t, d)$ is the flux of α flavor without neutrino oscillations, $p =$

$\cos^2 \theta_{12} \cos^2 \theta_{13}$ ($\sin^2 \theta_{13}$) is the survival probability for the normal (inverted) mass ordering in the adiabatic limit, E_ν is the neutrino energy, t is the time to collapse, d is the distance to the star, θ_{12} and θ_{13} are mixing angles. We employ this flux in estimating the number of IBD events in Section 3.2.

3. PRE-SUPERNOVA NEUTRINO DETECTION AND SN ALARM

In this section, we introduce neutrino detectors that could detect pre-SN neutrinos, and a scheme to estimate their detection ranges of distance and time. We then apply this scheme to the four pre-SN neutrino models with $15 M_\odot$ introduced in the previous section. We also discuss the current status and some future prospects of an SN alarm with pre-SN neutrinos.

3.1. Detectors and pre-SN neutrino observations

We first introduce the current and future detectors, mainly focusing on the detection of pre-SN neutrinos.

3.1.1. KamLAND. KamLAND is a 1-kt neutrino detector located at the Kamioka mine in Japan (67). KamLAND can detect pre-SN $\bar{\nu}_e$ events via IBD in low-background conditions, owing to the selection of a DC pair of prompt and delayed events with temporal and spatial correlations. The prompt event indicates scintillation light from the kinetic energy of positron and two 511-keV γ -rays via the pair annihilation of a positron and an electron. The delayed event is a 2.2-MeV γ -ray through neutron capture on a proton. This DC method can reject most accidental backgrounds.

Unavoidable backgrounds for pre-SN neutrinos are the terrestrial neutrinos emitted in the decays of nuclei in reactors and radionuclides throughout the Earth's interior. The largest uncertainty is due to the statuses of the reactors in Japan. The Great East Japan Earthquake in 2011 lowered the the reactor background. The background rate is 0.07 events/day, with a fiducial volume of ~ 0.7 kt in the energy range for pre-SN neutrinos, $0.9 \leq E_p \leq 3.5$ MeV (68). Here, E_p is the visible energy of the prompt signal. Before the earthquake, the background rate was 0.35 events/day.

The KamLAND collaboration evaluated the detection possibility of pre-SN neutrinos from nearby massive stars and found that KamLAND will detect pre-SN neutrinos from stars within 690 pc with the 3σ significance (68), assuming low-reactor backgrounds, based on the $25 M_\odot$ model developed by Odrzywolek & Heger (54).

3.1.2. SNO+. Sudbury Neutrino Observatory plus (SNO+) is an experiment intended to search for neutrino-less double- β decay of ^{130}Te , using the underground equipment already installed for SNO at SNOLAB in Sudbury, Canada (69). It is designed to use 780 t liquid scintillator. SNO+ will use IBD to detect pre-SN $\bar{\nu}_e$'s. Without ^{130}Te , the expected total number of reactor and geo-neutrino events with IBD is expected to be ~ 88.5 Terrestrial Neutrino Units (TNU), which corresponds one DC event per 10^{32} free protons per year (70), in a low energy region. Roughly speaking, the DC event rate from reactor and geo-neutrinos is about 0.16 events/day. This is the background rate for pre-SN neutrinos. Without Te, the sensitivity of SNO+ is similar to that of KamLAND. However, after loading Te, the sensitivity will become worse in SNO+ because of

the increase in accidental backgrounds through two-neutrino double- β decays of ^{130}Te .

3.1.3. JUNO. JUNO is a 20-kt multi-purpose underground liquid scintillator detector (71). It is designed to deploy a single (far) detector at baselines of ~ 53 km from both the Yangjiang and the Taishan reactors to confirm neutrino mass ordering and precisely measure oscillation parameters with reactor neutrinos. Pre-SN neutrinos can be detected via IBD at JUNO. The cumulative expected numbers of DC events on the last day before core collapse at $d = 1$ kpc are 6.1 (1.9), 12.0 (3.6), 20.5 (5.9) and 24.5 (7.0) for the normal (inverted) mass ordering using stellar models (20) with 12, 15, 20 and 25 M_{\odot} , respectively (72). This estimation assumes a detection efficiency of 0.83 and a $\bar{\nu}_e$ energy window of $1.8 \leq E_{\bar{\nu}_e} \leq 4$ MeV. The corresponding reactor and geo- $\bar{\nu}_e$ events are 15.7 and 1.1, respectively. If the distance to the source is known exactly, JUNO can determine the neutrino mass ordering at a $> 95\%$ confidence level for the stars located within 440–880 pc. It is, however, too optimistic to assume that this situation is realized, and other model-independent method is discussed with a combination of IBD and Electron Scattering (ES) events (72). If the cosmogenic backgrounds for the ES events will be reduced by a factor of 2.5–10, a model-independent determination of the neutrino mass ordering is possible with pre-SN neutrinos from Betelgeuse.

3.1.4. SK and SK-Gd. SK is a water Cherenkov detector located in the Kamioka mine in Japan, and IBD is available to detect $\bar{\nu}_e$'s (73). Unfortunately, the detection efficiency of delayed 2.2-MeV γ -rays through neutron capture on protons is only 17.74% for a supernova relic neutrino search (74). In addition, only a small part of a prompt event exceeds the detection threshold of 3.5 MeV in the electron kinetic energy and ~ 5.3 MeV in the neutrino energy. This is much larger than the threshold for IBD ($E_{\bar{\nu}_e} = 1.8$ MeV). Moreover, prompt events generated from pre-SN $\bar{\nu}_e$'s are, buried in backgrounds without the delayed events. Therefore, SK is not currently suitable for the detection of pre-SN neutrinos.

Recently, SK-Gd was approved. Neutrons produced through IBD are captured by Gd and 8-MeV γ -rays are released. These delayed events will be visible. However, the detection efficiency of prompt signals is still low, and the SK collaboration proposed two analyses for pre-SN neutrino events (5). One is the channel with DC events, even if only a small number of prompt events is visible. A typical selection efficiency of DC events is 3.9–6.7%, with a background rate of 24–56 events/day. The other is the analysis only for the delayed neutron events. The selection efficiency is estimated to be 7.3–10%, with a background rate of 132–280 events/day. Based on this analysis, the maximum detection range is ~ 600 pc with one false alarm per yr, assuming the normal mass ordering based on the 15 and 25 M_{\odot} models in Patton *et al.* (53). The first phase of SK-Gd will start with 10 tons of $\text{Gd}_2(\text{SO}_4)_3$ (0.01% Gd concentration) in 2020 (one-tenth of the final goal).

3.1.5. Dark matter detectors. Large dark matter experiments may potentially detect pre-SN neutrinos because of the combination of very low detection thresholds (around or below the keV level) and CE ν NS (19). One advantage in these experiments is a sensitivity to all six flavors of neutrinos, from which complementary observations of pre-SN neutrinos are expected. For example, a proposed argon detector with a target mass of 300 t and an energy threshold of 0.6 keV would detect 23.6 (68.4) events within a 12-hour time window before collapse of a

15 M_\odot (30 M_\odot) star at a distance within $d = 200$ pc. In such a configuration, the detection significance exceeds 3σ $\mathcal{O}(10)$ hours prior to collapse in the 30 M_\odot star, whereas the same situation is satisfied within an hour before collapse for the 15 M_\odot star.

3.1.6. DUNE. DUNE consists of four 10-kt liquid argon time projection chambers, located at SURF in South Dakota (75). It is designed as a far detector for the Long-Baseline Neutrino Facility (LBNF). The primary objectives of DUNE are to determine neutrino mass ordering, to measure a CP violation in the neutrino sector, and to measure supernova neutrino bursts after core bounce. Even so, DUNE will play an important role in pre-SN neutrino observations because it has the highest sensitivity to ν_e 's among all the currently planned neutrino detectors. In particular, DUNE will detect tens of thousands of charged current (CC) events before core bounce for the ECSN-progenitor with $M_{\text{ZAMS}} = 9 M_\odot$, assuming that the energy threshold is $E_\nu = 10.8$ MeV (16).

3.2. Detector sensitivity

The sensitivity of detectors to pre-SN neutrinos has been discussed in the literature (5, 14, 15, 16, 19, 68, 72). However, different studies have often used different pre-SN models, detection statistics, and/or time windows. Here, we present a unified method and discuss detector sensitivity with IBD on SK-Gd, KamLAND, and JUNO. In this study, we estimate the pre-SN $\bar{\nu}_e$ flux using eq.(10) with $\cos^2 \theta_{12} = 0.692$ and $\cos^2 \theta_{13} = 0.9766$ (76). To be technically accurate, we assume that $t = 0$ is the time, at which these studies stop the calculations of stellar evolutions. We regard this time as the onset of collapse. We also assume that the detector background rate is constant. Although we skip the sensitivity of DUNE and large dark matter detectors because of a lack of detailed information, DUNE has a unique advantage for pre-SN neutrino detection because it is sensitive to ν_e 's via CC interactions, while large dark matter detectors can detect all flavors of neutrinos.

An event rate at a time t is written as

$$R(t, d) = N_P \int F_{\bar{\nu}_e}(E_\nu, t, d) \sigma(E_\nu) \epsilon(E_\nu) dE_\nu, \quad (11)$$

where N_P is the number of target protons, $\sigma(E_\nu)$ is the cross section of IBD and $\epsilon(E_\nu)$ is the detection efficiency as a function of the neutrino energy E_ν . The time evolutions of $R(t, d)$ for the four pre-SN models at JUNO with $d = 200$ pc are shown in the top panel of Figure 4. The time profiles exactly show those of the number luminosities and average energies (i.e., the peaks associated with shell burnings) in Figure 3. We find that $R(t, d)$ is generally smaller than one and hence we have to discuss the pre-SN neutrino detection with a cumulative number of events defined as $\langle N_s(t, d) \rangle = \int_t^{t+t_w} R(t', d) dt'$, with a fixed time window of t_w . Here $\langle \cdot \cdot \cdot \rangle$ indicates the ensemble average with repeated measurements. We show the time evolution of $\langle N_s \rangle$ with $t_w = 24$ hr and $d = 200$ pc for the normal ordering in the bottom panel of Figure 4. In the Patton and Odrzywolek models, we find the steep gradient in $\langle N_s \rangle$ due to the shell burnings at $t \sim 2 - 3$ hr. In the Kato and Yoshida models, the $\langle N_s \rangle$'s have their extrema at $t \sim 20$ hr because they decrease after the peaks associated with shell burnings are out of the range for t_w .

The cumulative number of events $N(t)$ actually observed at neutrino detectors, follows the Poisson probability $P(N(t), N_{\text{ex}}(t, d))$, with an average $N_{\text{ex}}(t, d) = \langle N_s(t, d) \rangle + \langle N_b \rangle$, assuming

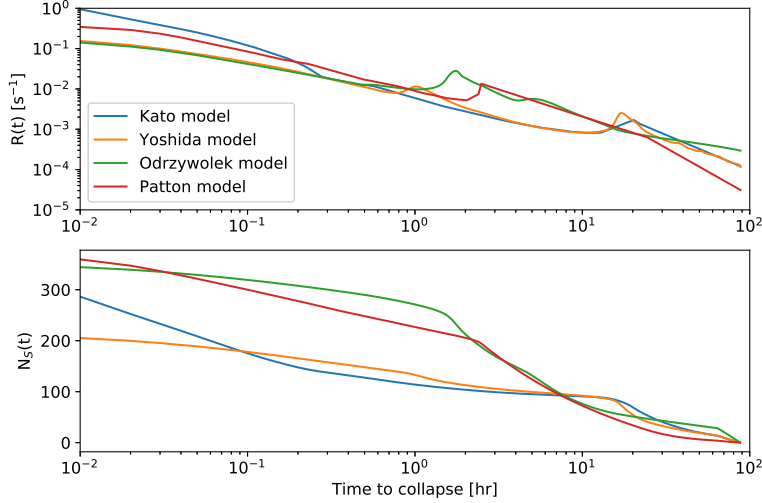


Figure 4

Time evolutions of event rates (top) and cumulative numbers of DC events (bottom) at JUNO. We adopt four pre-SN neutrino models (15, 16, 53, 54) to the estimation and assume that neutrinos have normal mass ordering. The time window is 24 hr, and the distance is 200 pc.

Table 1 Summary of detector parameters. Detector size is defined as the full volume for SK-Gd and JUNO and as the fiducial volume for KamLAND.

Detector name	Detector size	BG [event/day]	Efficiency	Estimation
SK-Gd (neutron)	32.5 kt	132	10%	Optimistic
SK-Gd (neutron)	32.5 kt	280	7.3%	Pessimistic
SK-Gd (DC)	32.5 kt	24	Black curve in Fig. 8 of Ref. (5)	Optimistic
SK-Gd (DC)	32.5 kt	56	Blue curve in Fig. 8 of Ref. (5)	Pessimistic
KamLAND	0.7 kt	0.07	Fig. 4 of Ref. (68)	Optimistic
KamLAND	0.7 kt	0.35	Fig. 4 of Ref. (68)	Pessimistic
JUNO	20 kt	16.8	0.73	

that $N(t_1)$ and $N(t_2)$ ($t_1 \neq t_2$) are independent. Here, $\langle N_b \rangle$ is the estimated number of background events with a time window of t_w . If we assume a 50% detection efficiency, the cumulative number of events $N_{50}(t, d)$ is defined with the given $N_{\text{ex}}(t)$ as

$$\int_0^{N_{50}(t, d)} P(N(t), N_{\text{ex}}(t, d)) dN = 0.5. \quad (12)$$

We then get an accidental detection probability $A(t, d)$ for $N_{50}(t, d)$,

$$A(t, d) = \int_{N_{50}(t, d)}^{\infty} P(N, \langle N_b \rangle) dN. \quad (13)$$

Generally, a false alarm rate per year, $F(t, d) = A(t, d) \times 365 \times 24/t_w$, is preferable for the discussion of the accidental detection to $A(t, d)$ itself.

Detector parameters used in this section are summarized in Table 1. We define detector size as the full volume for SK-Gd and JUNO and as the fiducial volume for KamLAND. We make optimistic (high detection efficiency and low backgrounds) and pessimistic (low detection efficiency and high backgrounds) estimations for SK-Gd from Reference (5). We also employ optimistic (low-reactor) and pessimistic (normal-reactor) background conditions for KamLAND. We consider only reactor and geo-neutrinos as the background for JUNO, although this assumption is less realistic than that for SK-Gd and KamLAND.

The left panels of Figure 5 show $F(d)$ at $t = 0.01$ hr for the Kato model as a function of distance in SK-Gd, KamLAND, and JUNO with $t_w = 12, 24$ and 48 hr. We assume that neutrinos have the normal ordering. Here, we focus on the time range $t > 0.01$ hr because the exact definition of $t = 0$ is uncertain and depends on models as we mentioned. For SK-Gd, we assume $F_{\text{SK}}(t, d) = A_n(t, d)A_{\text{DC}}(t, d) \times 365/t_w$, where $A_n(t, d)$ and $A_{\text{DC}}(t, d)$ are the accidental detection probabilities for only neutron events and DC events, respectively. If we require $F(t, d) = 1 \text{ yr}^{-1}$ for a detection, SK-Gd and KamLAND have a similar sensitivity to pre-SN neutrinos and have enough capability to predict the supernova explosion of Betelgeuse (200 pc) before collapse. JUNO has the highest sensitivity, and the distance can be extended to ~ 1 kpc. Regarding the capabilities of an SN alarm with pre-SN neutrinos, the right panels of Figure 5 show $F(t)$ as a function of time to collapse, assuming that the Betelgeuse supernova occurs at $d = 200$ pc. The earliest alarm will be triggered by the detection at JUNO ~ 78 hr prior to collapse, when $F(t, d) = 1 \text{ yr}^{-1}$. KamLAND is preferable for triggering an early alarm to SK-Gd for the Kato model.

Previous studies have employed windows of $t_w = 12$ and 48 hr in estimating false alarm rates for SK-Gd and KamLAND, respectively. An optimization of t_w is, however, unclear. Even focusing on SK-Gd, the longest detection distance is derived when $t_w = 12$ hr, whereas the best t_w for the alarm time depends on the models considered. The most promising t_w , moreover, depends on detectors. Actually, the detection distance becomes the longest in the case of $t_w = 48$ hr at KamLAND. It is obvious that $\langle N_s \rangle$ and $\langle N_g \rangle$ increase with a time window t_w , and the most promising t_w is determined by keeping a balance between their increments with t_w . At KamLAND, the low $\langle N_g \rangle$ is achieved even for $t_w = 48$ hr, and it provides us the best sensitivity. The shorter the time window is, the more promising at SK-Gd because of the higher $\langle N_g \rangle$. JUNO has intermediate properties between SK-Gd and KamLAND.

Table 2 summarizes the detection ranges and alarm times, where the false alarm rate $F(t)$ is 1 yr^{-1} , for the four $15 M_\odot$ models. Roughly speaking, the detector sensitivity in SK-Gd and KamLAND is similar. Even so, KamLAND with $t_w = 48$ hr has a better configuration for the alarm time. A 35–45% uncertainty of the detection ranges in pre-SN neutrino models is seen, even if their ZAMS mass is fixed to $15 M_\odot$. The uncertainty of the alarm times is much larger. In the worst case, the alarm time at KamLAND has a range from 7.5–13 hr ($t_w = 48$ hr, Patton model) to 17–26 hr ($t_w = 48$ hr, Kato model) for the normal ordering. The dependence of the mass ordering is also important. For the Kato and Yoshida models, it is difficult to realize an early alarm with the inverted ordering at SK-GD and KamLAND. In contrast, KamLAND will be able to detect pre-SN signals 15–26 hr before collapse with $t_w = 48$ hr in the normal ordering. Because the Odrzywolek and Patton models have similar numbers of DC events at KamLAND

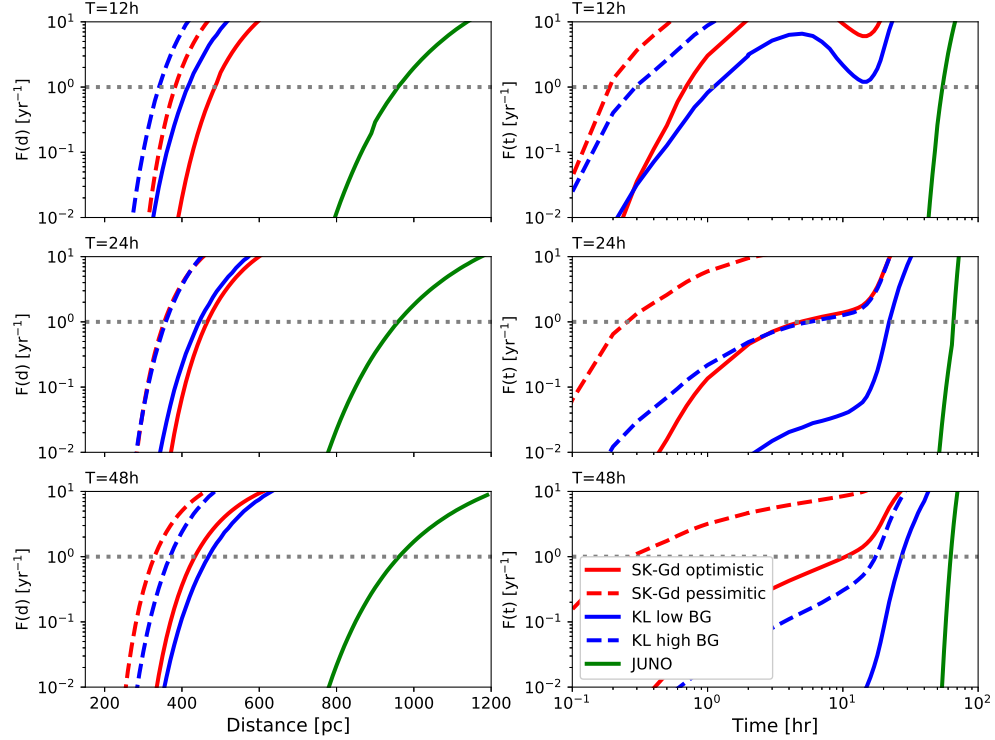


Figure 5

False alarm rate as a function of distance (left) and time (right) with the Kato model (16) for normal mass ordering. It is assumed that the supernova occurs at 200 pc in the right panels. The time windows are defined as $t_w=12, 24$ and 48 hr from top to bottom. The dotted lines show a false alarm rate with 1 yr^{-1} .

with $t_w = 48$ hr, their detection ranges are also similar. The alarm times are, however, quite different; 11 – 38 hr in the Odrzywolek model and 7.5 – 13 hr in the Patton model. To discuss the detection time, we have to pay attention not only to the $\langle N_s \rangle$ itself but also to its time evolution. Among all the models, JUNO has the best sensitivity to pre-SN neutrinos. The detection range reaches 810 – 1030 pc, and we can predict the Betelgeuse supernova 38 – 74 hr prior to the collapse for the normal ordering with $t_w = 48$ hr depending on models. Here, we estimate the detection ranges and the alarm times for $t < 88$ hr over the time window used for the Kato model calculation. Therefore, the sensitivity of JUNO should be improved by the longer calculations of pre-SN neutrinos. Also, we use four $15 M_\odot$ models in this study, assuming Betelgeuse-like targets. If we consider more massive stars, the detection range and alarm time will be enhanced (68, 5, 72).

Finally, it should be noted that we have not considered the actual detector responses (e.g.,

the energy resolution and quenching) in this work because these responses may not have made a significant difference in the previous studies of SK-Gd (5) and KamLAND (68).

Table 2 Detection ranges and alarm times for normal (inverted) mass ordering, where a false alarm rate is 1 yr^{-1} , for four pre-SN neutrino models with $15 M_{\odot}$.

Detector	Model	$N_s^{\text{DC}}(t = 0.01)$	Detection range [pc]	Alarm time [hr]	t_w [hr]
SK-Gd	Kato	46.7–49.9 (10.9–11.7)	380–480 (180–230)	0.1–0.6 (–0.02)	12
		50.8–54.3 (12.2–13.0)	350–460 (170–220)	0.2–4.5 (–0.02)	24
		54.3–58.0 (13.3–14.3)	320–430 (160–210)	0.2–10 (–0.01)	48
	Yoshida	21.4–22.8 (12.4–13.2)	260–330 (190–250)	0.1–1 (–0.1)	12
		26.3–28.0 (15.0–16.0)	260–340 (190–260)	0.4–6 (–0.2)	24
		28.4–30.2 (16.1–17.2)	240–320 (180–240)	0.2–6.5 (–0.2)	48
	Odrzywolek	45.3–48.3 (12.8–13.7)	380–490 (200–260)	4–6.5 (0.02–1.7)	12
		47.3–50.4 (13.4–14.3)	340–460 (180–240)	3–6.5 (–1.6)	24
		49.1–52.4 (14.0–14.9)	310–420 (170–220)	3–7 (–0.7)	48
	Patton	43.5–46.3 (12.9–13.9)	370–480 (200–260)	3.5–6 (0.02–0.9)	12
		45.8–48.9 (13.8–14.7)	340–450 (180–250)	3–6.5 (–0.5)	24
		46.8–49.8 (14.1–15.0)	310–410 (170–220)	2.5–5.5 (–0.1)	48
KamLAND	Kato	7.6 (1.6)	340–410 (150–190)	0.2–1 (NA)	12
		9.3 (2.1)	350–440 (170–210)	5.5–20 (–0.02)	24
		10.9 (2.6)	360–460 (180–220)	17–26 (–0.1)	48
	Yoshida	4.5 (2.4)	260–310 (190–230)	0.5–16 (–0.1)	12
		6.5 (3.5)	290–370 (210–270)	8–18 (0.1–1.8)	24
		7.7 (4.1)	310–390 (220–280)	15–22 (0.3–7.5)	48
	Odrzywolek	9.7 (2.8)	380–460 (200–240)	5.5–8 (0.04–1.7)	12
		11.0 (3.1)	380–480 (200–250)	7–13 (0.08–2)	24
		12.4 (3.5)	390–490 (200–260)	11–38 (0.1–2.5)	48
	Patton	10.1 (2.9)	390–470 (200–250)	5.5–8.5 (0.07–1.9)	12
		11.4 (3.5)	390–490 (210–260)	7–11 (0.1–2.5)	24
		12.2 (3.6)	380–490 (210–260)	7.5–13 (0.1–3)	48
JUNO	Kato	232 (48.7)	950 (430)	54 (24)	12
		286 (65.2)	950 (440)	64 (28)	24
		341 (81.8)	960 (470)	62 (34)	48
	Yoshida	142 (75.7)	740 (540)	52 (30)	12
		205 (109)	810 (590)	64 (38)	24
		247 (131)	810 (590)	62 (46)	48
	Odrzywolek	303 (86.2)	1090 (580)	78 (14)	12
		344 (97.8)	1050 (560)	76 (28)	24
		391 (111)	1030 (540)	74 (48)	48
	Patton	315 (90.6)	1110 (590)	30 (17)	12
		360 (106)	1070 (580)	34 (19)	24
		385 (115)	1020 (550)	38 (20)	48

3.3. Early alarm with pre-supernova neutrino

Recently, some projects attempt to realize an SN alarm with pre-SN neutrinos. In this section, we give some examples of such activities.

3.3.1. Alarm system at KamLAND. KamLAND launched an alarm system with pre-SN neutrinos in 2015⁴. Signals from photomultiplier tubes are first digitized, and the energies of the events are reconstructed in the manner of the standard analysis at KamLAND. It should be noted that KamLAND uses tentative calibration values and dead time tables in this process, for which a dedicated analysis is required. Finally, the detection significance is calculated and released online. The entire process takes ~ 25 min, but it is possible to announce the detection in real time. Registration and authorization are required for access to the detection significance. The KamLAND collaboration is planning to implement an alarm distribution via the Gamma-ray Coordinates Network (GCN)⁵.

3.3.2. Alarm with SNEWS2.0. Besides KamLAND, new detectors with high sensitivity to pre-SN neutrinos (e.g. SK-Gd, SNO+ and JUNO) will be running in the next few years. An alarm system with multiple neutrino detectors will be realized soon, which will help prevent nearby SNe from escaping detection. In addition, future detectors will have various detection channels, which will make it possible to detect all flavors of neutrinos and to perform multi-flavor studies for neutrino sources. The “SuperNova Early Warning System (SNEWS)” is one such candidate (77). SNEWS involves an international collaboration representing current supernova neutrino-sensitive detectors (SK, LVD, IceCube, KamLAND, Borexino, DayaBay, and HALO). It aims to provide the astronomy community with a prompt alarm for galactic supernovae, since neutrino signals emerge in the early stages of a supernova explosion. SNEWS is scheduled for an upgrade to SNEWS2.0, in which pre-SN neutrinos will be covered.

4. FINDINGS FROM FUTURE OBSERVATIONS

As discussed in the previous section, observations of pre-SN neutrinos have come into view. In this section, we then move on to the discussion about what we can learn from future observations of pre-SN neutrinos. We introduce three findings: distinction of progenitor models, restriction on convective properties, and determination of neutrino mass ordering.

4.1. Distinction of progenitor models for core-collapse supernovae

A CCSN’s progenitor type is one of key determinants of its stellar evolution. There are two types of progenitors leading to ECSNe and FeCCSNe, as discussed in Section 2.1. The boundary for the initial mass between the two progenitors is still unknown (22, 24, 29). The thermal evolutions of their cores are quite different because of the degree of degeneracy of electrons. In Figure 1, the $9 M_{\odot}$ ECSN-progenitor is cooled via neutrino emission efficiently after carbon burning, and the central temperature becomes much lower than those in 12, 15 and $20 M_{\odot}$ progenitors of FeCCSNe, for which the central temperatures increase continuously up to the onset of collapse. The temperature rises rapidly in association with the O+Ne deflagration, which is a key feature of the ECSN-progenitor.

⁴<https://www.awa.tohoku.ac.jp/kamland/SNmonitor/regist/index.html>

⁵<https://gcn.gsfc.nasa.gov>

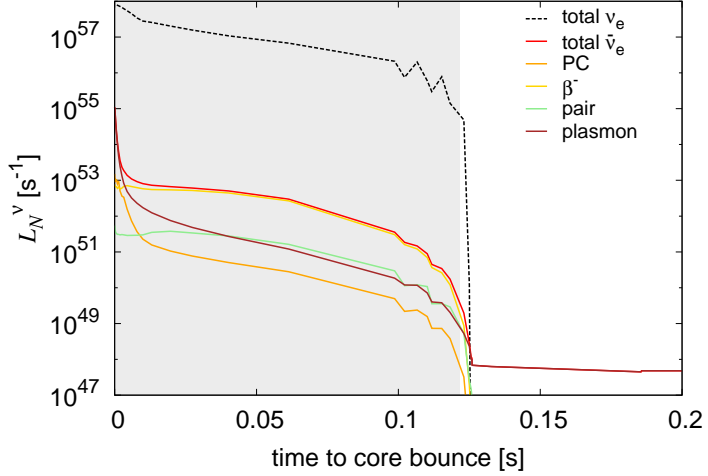


Figure 6

Time evolution of number luminosities for the $9 M_{\odot}$ ECSNe-progenitor (16). The gray area represents the deflagration phase. Neutrino oscillations are not included.

Table 3 Expected numbers of detection events until core bounce^{a,b}. Numbers are pertinent to ν_e 's for DUNE and to $\bar{\nu}_e$'s for JUNO. In the case of the $15 M_{\odot}$ FeCCSN-progenitor, the individual contributions from the progenitor and collapse phases are also shown in that order in parentheses. The source is assumed to be located at 200 pc from the Earth. Data from Kato *et al.* (16).

detector	$9 M_{\odot}$		$15 M_{\odot}$	
	normal	inverted	normal	inverted
JUNO	0.98	0.04	894	204
			(891+3.07)	(203+0.63)
DUNE	1765	22685	169	2142
(5MeV)			(57.8+111)	(713+1429)
DUNE	1238	15910	69.3	895
(10.8MeV)				

^aBackground noise was neglected in these estimations.

^bTable 2 focuses on the time window for 0.1 hr before the core bounce; in this table, the event rates are integrated over a whole time range of progenitor and collapsing phases.

Kato *et al.* (14) employed state-of-the-art stellar evolution models and calculate pre-SN emissivity via pair annihilation and plasmon decay. In a follow-up article (16), they broadened the scope to include all flavors of neutrinos emitted from the pre-bounce phase. The time evolutions of the number luminosities for the $15 M_{\odot}$ FeCCSN-progenitor and the $9 M_{\odot}$ ECSN-progenitor are shown in Figures 2 and 6, respectively. The number luminosity in the FeCCSNe-progenitor gradually increases from a few days before core bounce, whereas the number luminosity in the

ECSNe-progenitor drastically increases at $t = 125$ ms because of the O+Ne deflagration (see gray shaded region in Figure 6). The deflagration wave propagates outward to produce the NSE behind, and β^- decay and ECs on heavy nuclei as well as on free protons efficiently emit $\bar{\nu}_e$'s and ν_e 's.

The expected numbers of neutrino events at JUNO and DUNE are summarized in Table 3, in which it is assumed that the progenitors are located at 200 pc. These estimations include neutrinos emitted in the collapse phase and neglect background noises in neutrino detectors discussed in the previous section. It is found that JUNO can detect a few tens of $\bar{\nu}_e$'s from the FeCCSN-progenitor, even if they are emitted from 1 kpc away. The detection of $\bar{\nu}_e$'s from the ECSN-progenitor seems to be nearly impossible, even with the planned detector. We will hence be able to distinguish the two types of progenitors by detection or non-detection of $\bar{\nu}_e$'s. Kato *et al.* (16) also estimated the expected numbers of ν_e events for the two values of the energy thresholds, 5 and 10.8 MeV, at DUNE. The energy of ν_e 's in the collapse phase is high (~ 8 MeV), and we will still be able to detect a large number of ν_e 's. This implies that irrespective of the type and mass of the progenitor, we may be able to confirm our current understanding of the physics in the collapse phase.

4.2. Restriction on convective properties

Convections caused by the large energy generation in nuclear burnings affect the mixing of products and, in turn, change the core mass. A slight change in mass induces drastic change in the dynamics of the core, and convective properties are hence one of the key phenomena in the stellar evolution. Our knowledge about these properties is, however, limited, and their theoretical treatment presents a large obstacle. It is possible that pre-SN neutrino observations may provide clues to help solve this problem (15).

Figure 7 shows the time evolution of neutrino events at JUNO (left), SK-Gd (middle) and HK-Gd (right). There are two peaks at ~ 17 and 2 hr before core collapse, which correspond respectively to the ignitions of O-shell and Si-shell burnings. The central temperature and density decrease because of the core expansion at the onsets of shell burnings, and these decreases lead to the suppression of neutrino emission in the core. From the observational perspective, $\bar{\nu}_e$'s emitted at the core have a larger contribution because they have high energies. The number of neutrino events is hence reduced because of shell burnings. Such features in neutrino events will confirm the existence of shell burnings, and provide information regarding this phenomenon (i.e., duration of shell burnings).

4.3. Determination of neutrino mass ordering

The observations of pre-SN neutrinos may help in determining the yet-known neutrino mass ordering. Because the behavior of the neutrino oscillation depends on the neutrino mass ordering, the number of neutrino events differ between the mass orderings. In principle, we will be able to detect more than a thousand ν_e 's at DUNE, if the distance to the source is 200 pc and if neutrinos have the inverted mass ordering. In contrast, the event numbers are reduced by a factor of ~ 10 if they obey the normal mass ordering (16).

Guo *et al.* (72) suggested a model-independent method to determine the mass ordering

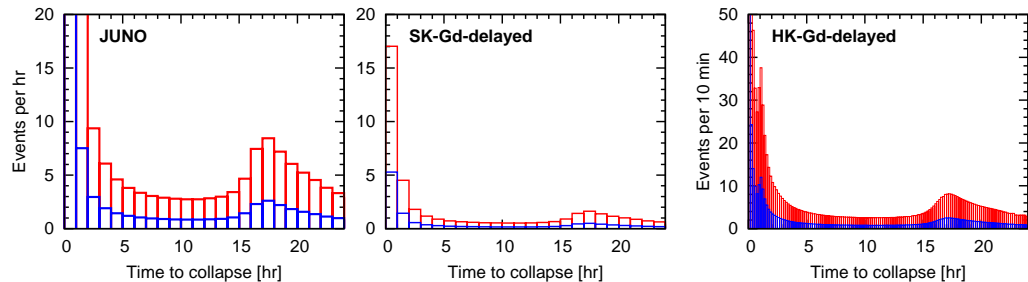


Figure 7

Expected numbers of $\bar{\nu}_e$ events for the Yoshida model (15) with $15 M_{\odot}$ at JUNO, SK-Gd and HK-Gd from left to right. Events are measured per 1 hr for JUNO and SK-Gd and 10 min for HK-Gd. Red and blue bars indicate normal and inverted mass orderings, respectively. Detector parameters for JUNO and SK are shown in Table 1. The detector efficiency for HK is assumed to be 0.5.

using the numbers of IBD and ES events, N_{IBD} and N_{ES} . Note that IBD is sensitive only to $\bar{\nu}_e$'s, whereas all flavors can be detected via ES. The $N_{\text{ES}}/N_{\text{IBD}}$ ratio is ~ 0.91 and ~ 3.8 at JUNO for the normal and inverted orderings, respectively, assuming pre-SN neutrinos are emitted from Betelgeuse. Guo *et al.* found that this large difference in $N_{\text{ES}}/N_{\text{IBD}}$ ratio between the normal and inverted orderings is insensitive to stellar models. These facts provide the basis for a model-independent determination of mass ordering. Although the current background rate for ES events is too high to perform this method, future reduction of backgrounds will make it possible.

5. SUMMARY AND FUTURE PROSPECTS

5.1. Summary

Almost 30 years have passed since the historical supernova neutrino events of SN 1987A. Remarkable progress has been made in neutrino detection techniques, opening neutrino astronomy to a new target, pre-SN neutrinos, which are mainly emitted from the cores of massive stars before core bounce. This possibility was first pointed out by Odrzywolek *et al.* (13), and followed by many works with state-of-the-art calculations of stellar evolutions. Uncertainties in stellar physics will be clarified by pre-SN neutrino observations because neutrinos freely propagate through stars. Their signals, moreover, issue a SN alarm for a few days before a supernova explosion and enable us to observe it. In this review, we have introduced pre-SN neutrinos from both the theoretical and observational points of view.

Massive stars evolve by repeating the cycle of nuclear burning and gravitational core contraction until the ONe core is formed. A stellar subsequent evolution depends on the ONe core mass; massive stars evolve into ECSNe or FeCCSNe depending on the initial mass. Neutrinos have an important role in the thermal evolutions of the core. In the case of the Kato model for the $15 M_{\odot}$ FeCCSN-progenitor, the number luminosity of ν_e 's gradually increases up to

$L_N^\nu \sim 10^{55}$ and 10^{57} s^{-1} just before core collapse and core bounce, respectively. ECs on heavy nuclei and free protons make large contributions to the total ν_e luminosity. For $\bar{\nu}_e$'s, on the other hand, their number luminosity reaches a maximum $L_N^\nu \sim 10^{53} \text{ s}^{-1}$ at the beginning of core collapse. Neutrino emission via pair annihilation dominates the other reactions at $t > 400 \text{ s}$, whereas after this, β^- decay overcomes it. The average energies are ~ 8 and 3 MeV for ν_e 's and $\bar{\nu}_e$'s, respectively. These properties of pre-SN neutrinos depend on stellar models and neutrino processes taken into account. The peaks of number luminosities vary in amplitude and width, even if the initial mass is fixed and the investigation of the progenitor dependence is therefore strongly required. In any case, pre-SN neutrinos are smaller in number and have lower energies than do SN neutrinos, and detectors should have high sensitivity to low-energy neutrinos and a low background for the detection of pre-SN neutrinos.

Various channels are currently employed in neutrino detection, and this variety makes it possible to detect multi-flavor neutrinos. In detectors, considerable efforts have been made to reduce background noises, and the detection of pre-SN neutrinos come into view. Detector sensitivity regarding pre-SN neutrinos has been discussed for different pre-SN models, detection statistics, and time windows. We have hence presented a unified method for detector sensitivity with IBD on SK-Gd, KamLAND and JUNO and performed a comprehensive study using representative pre-SN neutrino models. We have found that JUNO has the greatest sensitivity to pre-SN neutrinos and can detect pre-SN neutrinos from progenitors even at $\sim 1 \text{ kpc}$. SK and KamLAND, on the other hand, have a similar sensitivity and will predict the explosion of Betelgeuse at 200 pc . We have also discussed an SN alarm for the same target and have found that JUNO will be able to issue an alarm $\sim 78 \text{ hr}$ prior to collapse. The detection range and alert time depend on a time window t_w for the cumulative number of events and pre-SN neutrino models. The most promising t_w is determined by keeping a balance between the increments of $\langle N_s \rangle$ and $\langle N_g \rangle$ with t_w . The longer t_w provides better sensitivity at KamLAND because of the low background rates, whereas the sensitivity of SK reaches its maximum with the shortest t_w . JUNO has intermediate dependence between those of SK-Gd and KamLAND. There is 35 – 45% uncertainty of the detection range in the pre-SN neutrino models, even if their ZAMS mass is fixed at $15 M_\odot$. The alarm times have a larger uncertainty. In the worst case for the normal ordering, the alarm time at KamLAND has a range from 7.5–13 hr ($t_w = 48 \text{ hr}$, Patton model) to 17–26 hr ($t_w = 48 \text{ hr}$, Kato model).

The importance of pre-SN neutrinos has been discussed in three points so far: distinction of progenitor models for CCSNe, restriction on convective properties, and determination of neutrino mass ordering. Firstly, Kato *et al.* (14, 16) found that we can distinguish two types of progenitors in CCSNe—FeCCSNe and ECSNe—by the detection or non-detection of $\bar{\nu}_e$'s. The thermal evolutions of these progenitors are quite different in the late phase because of the difference in the degeneracy of electrons, and the distinction of progenitors is important in establishing the stellar evolution theory. Secondly, shell burning, another important phenomenon, is also found in neutrino signals. Yoshida *et al.* (15) found two peaks in the time evolution of neutrino signals due to the suppression of neutrino emission by the onsets of O-shell and Si-shell burnings. The pre-SN neutrino observations will provide information about the properties of shell burnings (i.e., duration). Finally, observations of pre-SN neutrinos may help in determining the yet-known neutrino mass ordering. The neutrino fluxes at the Earth depend on the mass ordering because of neutrino oscillations, as shown by the difference ratios in the number of ES to IBD events. The

$N_{\text{ES}}/N_{\text{IBD}}$ ratio is ~ 0.91 and 3.8 at JUNO for the normal and inverted orderings, respectively, assuming pre-SN neutrinos are emitted from Betelgeuse. Such a large difference between mass orderings is model-independent and future measurements of this ratio will hence reveal the mass ordering.

5.2. Future prospects

Theoretical studies of pre-SN neutrinos have just started, and much remains to be done for the future pre-SN neutrino observations. Systematical studies using progenitors with various initial masses are the first priority. Within the detectable range for pre-SN neutrinos < 1 kpc from the Earth (see Table 2), there are 41 candidate RSGs, which are summarized in Table 4 (see Nakamura *et al.* (78) and references therein). Their initial masses are expected to be within a range of $9 - 25 M_{\odot}$, although it is difficult to determine them from observations. The evolution of a massive star is highly dependent on its initial masses (see the right panels of Figure 8) and we should hence take this dependence into account in the prediction of pre-SN neutrinos. Actually, we find that the number luminosities in both flavors differ by more than a factor of 10 with the initial mass. The left panels of Figure 8 show the number luminosities of ν_e 's (top) and $\bar{\nu}_e$'s (bottom). We also find that the number luminosities have positive and negative correlations with the central temperature and degeneracy of electrons in the middle and bottom panels on the right. These correlations may provide clues for stellar physics in the future. We should proceed with such theoretical studies to get precise information from the future observations.

Table 4 RSGs within 1 kpc from the Earth. Data from Nakamura *et al.* (78) and reference therein.

RSG	distance (pc)	RSG	distance (pc)	RSG	distance (pc)	RSG	distance (pc)
ϵ Peg	150	h^1 Pup	420	V424 Lac	600	HD203338	870
α Sco	160	145 CMa	440	HD217694	600	SW Cep	870
λ Vel	190	1 Pup	440	ES And	600	V557 Cep	870
ζ Cep	200	σ CMa	480	ψ^1 Aur	710	μ Cep	870
α Ori	220	o^1 CMa	480	41 Gem	710	RT Cep	870
q Car	360	BM Sco	480	HR5742	710	VV Cep	870
119 Tau	370	HR3692	540	HR8248	790	AZ Cep	870
w Car	390	12 Peg	600	ST Cep	790	CK Cep	870
47 Cyg	390	5 Lac	600	θ Del	860	V809 Cas	870
ξ Cyg	390	V418 Lac	600	V419 Cep	870	MY Gem	1000
						HR861	1000

From the observational point of view, the first priority is to establish an alarm system with multiple neutrino detectors. Detection at multi-detectors makes observational data reliable and more precisely imposes observational constraints on the stellar evolution and the explosion mechanism. In particular, the data derived from the detectors with sensitivity to different neutrino flavors broaden our findings. We may, moreover, point to neutrino sources using the neutrino detectors at different locations (79). Hence, there is a strong need to establish a combined-alarm system with multi-detectors such, as the SNEWS project.

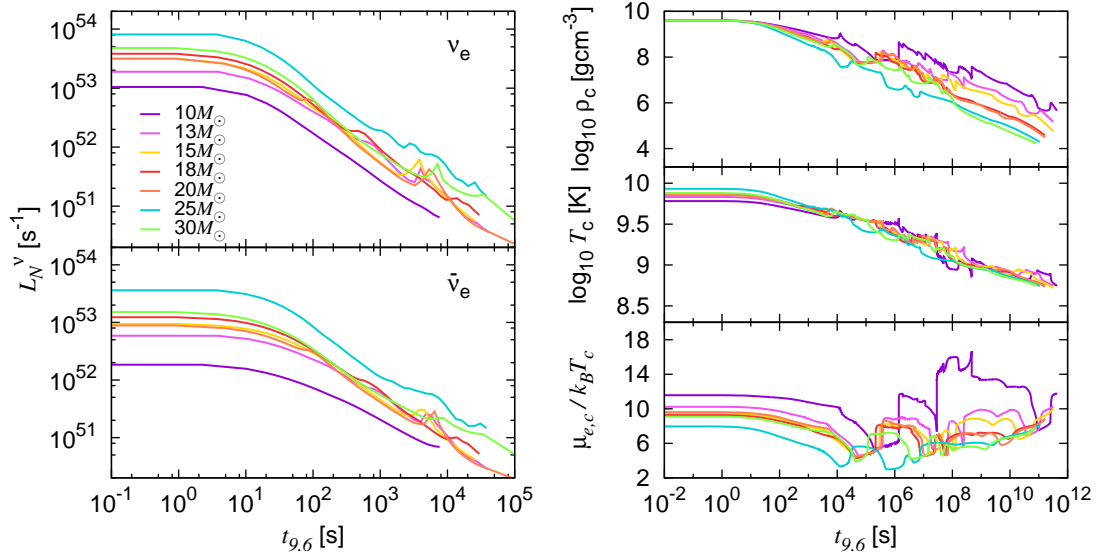


Figure 8

Left: Time evolutions of number luminosities of ν_e 's (top) and $\bar{\nu}_e$'s (bottom) for seven progenitor models with different initial masses in Set M_A (57). Neutrino oscillations are not included. Right: Time evolutions of the central density, temperature, and degeneracy of electrons, where $\mu_{e,c}$ is the electron chemical potential at the center and k_B is the Boltzmann constant. The origin of the time is defined when the central density becomes $\rho_c = 10^{9.6} \text{ g cm}^{-3}$.

ACKNOWLEDGMENTS

The writing of this review was supported by the Grant-in-Aid for Scientific Research on Innovative Areas (No. 26104007, 19H05803) from the Ministry of Education, Culture, Sports, Science and Technology and the Grant-in-Aid for the Scientific Research of Japan Society for the Promotion of Science (No. JP17H01130). C.K. is supported by Tohoku University Center for Gender Equality Promotion (TUMUG) Support Project (Project to Promote Gender Equality and Female Researchers). We would like to thank Editage (www.editage.com) for English language editing.

LITERATURE CITED

1. Hirata K, et al. *Phys. Rev. Lett.* 58:1490 (1987)
2. Bionta RM, et al. *Phys. Rev. Lett.* 58:1494 (1987)
3. Alekseev EN, Alekseeva LN, Volchenko VI, Krivosheina IV. *JETP Lett.* 45:589 (1987), [739(1987)]
4. Sato K, Suzuki H. *Phys. Rev. Lett.* 58:2722 (1987)
5. Simpson C, et al. *Astrophys. J.* 885:133 (2019)
6. Zuber K. *Nuclear and Particle Physics Proceedings* 265-266:233 (2015), proceedings of the Neutrino Oscillation Workshop
7. Acciarri R, et al. arXiv:1601.05471 [physics.ins-det] (2016)
8. Akimov D, et al. *Science* 357:1123 (2017)

9. Abe K, et al. *Astroparticle Physics* 89:51 (2017)
10. Lang RF, et al. *Phys. Rev. D* 94:103009 (2016)
11. Kozynets T, Fallows S, Krauss CB. *Astroparticle Physics* 105:25 (2019)
12. Smartt SJ. *Pub. Astron. Soc. Aust.* 32:e016 (2015)
13. Odrzywolek A, Misiaszek M, Kutschera M. *Astropart. Phys.* 21:303 (2004)
14. Kato C, et al. *Astrophys. J.* 808 (2015)
15. Yoshida T, Takahashi K, Umeda H, Ishidoshiro K. *Phys. Rev. D* 93 (2016)
16. Kato C, et al. *Astrophys. J.* 848 (2017)
17. Patton KM, Lunardini C, Farmer RJ. *Astrophys. J.* 840:2 (2017)
18. Odrzywolek A. *Phys. Rev. C* 80:045801 (2009)
19. Raj N, Takhistov V, Witte SJ. *Phys. Rev. D* 101:043008 (2020)
20. S. E. Woosley and A. Heger and T. A. Weaver. *Rev. Mod. Phys.* 74:1015 (2002)
21. Langer N. *Ann. Rev. Astron. Astrophys.* 50:107 (2012)
22. Doherty CL, Gil-Pons P, Siess L, Lattanzio JC. *Pub. Astron. Soc. Aust.* 34:e056 (2017)
23. Umeda H, Yoshida T, Takahashi K. *Prog. Theor. Exp. Phys.* 2012:01A302 (2012)
24. Jones S, et al. *Astrophys. J.* 772:150 (2013)
25. Takahashi K, Yoshida T, Umeda H. *Astrophys. J.* 771:28 (2013)
26. Doherty CL, et al. *Mon. Not. R. Astron. Soc.* 446:2599 (2015)
27. Crowther PA. *Ann. Rev. Astron. Astrophys.* 45:177 (2007)
28. Nomoto K, Hashimoto M. *Phys. Rep.* 163:13 (1988)
29. Woosley SE, Heger A. *Astrophys. J.* 810:34 (2015)
30. Suwa Y, et al. *Mon. Not. R. Astron. Soc.* 454:3073 (2015)
31. Nomoto K. *Astrophys. J.* 277:791 (1984)
32. Schwab J, Quataert E, Bildsten L. *Mon. Not. R. Astron. Soc.* 453:1910 (2015)
33. Suwa Y, et al. *Mon. Not. R. Astron. Soc.* 481:3305 (2018)
34. Siess L. *Astron. Astrophys.* 512:A10 (2010)
35. Miyaji S, Nomoto K, Yokoi K, Sugimoto D. *Pub. Astron. Soc. Jpn* 32:303 (1980)
36. Takahashi K, et al. *Astrophys. J.* 871:153 (2019)
37. Jones S, et al. *Astron. Astrophys.* 593:A72 (2016)
38. Leung SC, Nomoto K. *Pub. Astron. Soc. Aust.* 36:e006 (2019)
39. Itoh N, Hayashi H, Nishikawa A, Kohyama Y. *Astrophys. J. Suppl.* 102:411 (1996)
40. Guo G, Qian YZ. *Phys. Rev. D* 94:043005 (2016)
41. Mezzacappa A, Bruenn SW. *Astrophys. J.* 410:740 (1993)
42. Schinder PJ, Shapiro SL. *Astrophys. J. Suppl.* 50:23 (1982)
43. Braaten E, Segel D. *Phys. Rev. D* 48:1478 (1993)
44. Fuller GM, Fowler WA, Newman MJ. *Astrophys. J.* 293:1 (1985)
45. Oda T, et al. *At. Data Nucl. Data Tables* 56:231 (1994)
46. Langanke K, Martínez-Pinedo G. *At. Data Nucl. Data Tables* 79:1 (2001)
47. Langanke K, et al. *Phys. Rev. Lett.* 90:241102 (2003)
48. Langanke K, Martínez-Pinedo G, Sampaio JM. *Phys. Rev. C* 64:055801 (2001)
49. Sullivan C, et al. *Astrophys. J.* 816:44 (2016)
50. Bruenn SW. *Astrophys. J. Suppl.* 58:771 (1985)
51. Nagakura H, et al. *Astrophys. J.* 854:136 (2018)
52. <https://zenodo.org/record/3768052#.Xqr5ssj7SF4>
53. Patton KM, Lunardini C, Farmer RJ, Timmes FX. *Astrophys. J.* 851:6 (2017)
54. Odrzywolek A, Heger A. *Acta Phys. Polon.* B41:1611 (2010)
55. Takahashi K, et al. *Mon. Not. R. Astron. Soc.* 456:1320 (2016)
56. Takahashi K, Yoshida T, Umeda H. *Astrophys. J.* 857:111 (2018)

57. Yoshida T, et al. *Astrophys. J.* 881:16 (2019)
58. Farmer R, et al. *Astrophys. J. Suppl.* 227:22 (2016)
59. Furusawa S, Sumiyoshi K, Yamada S, Suzuki H. *Astrophys. J.* 772:95 (2013)
60. Wallace J, Burrows A, Dolence JC. *Astrophys. J.* 817:182 (2016)
61. Smy MB, et al. *Phys. Rev.* D69:011104 (2004)
62. Ashie Y, et al. *Phys. Rev.* D71:112005 (2005)
63. Abe K, et al. *Phys. Rev. Lett.* 112:181801 (2014)
64. Wolfenstein L. *Phys. Rev. D* 17:2369 (1978)
65. Duan H, Fuller GM, Qian YZ. *Annual Review of Nuclear and Particle Science* 60:569 (2010)
66. Dighe AS, Smirnov AY. *Phys. Rev.* D62:033007 (2000)
67. Suzuki A. *European Physical Journal C* 74:3094 (2014)
68. Asakura K, et al. *Astrophys. J.* 818:91 (2016)
69. Andringa S, et al. *Adv. High Energy Phys.* 2016:6194250 (2016)
70. Baldoncini M, et al. *Journal of Physics: Conference Series* 718 (2016)
71. An F, et al. *Journal of Physics G Nuclear Physics* 43:030401 (2016)
72. Guo G, Qian YZ, Heger A. *Phys. Lett.* B796:126 (2019)
73. Abe K, et al. *Nuclear Instruments and Methods in Physics Research A* 737:253 (2014)
74. Zhang H, et al. *Astropart. Phys.* 60:41 (2015)
75. Acciarri R, et al. *arXiv e-prints* :arXiv:1601.05471 (2016)
76. Olive KA, et al. *Chin. Phys.* C38:090001 (2014)
77. Antonioni P, et al. *New Journal of Physics* 6:114 (2004)
78. Nakamura K, et al. *Mon. Not. R. Astron. Soc.* 461:3296 (2016)
79. Linzer NB, Scholberg K. *Phys. Rev. D* 100:103005 (2019)